Nano Research

ISSN 1998-0124 CN 11-5974/O4
https://doi.org/10.1007/s12274-023-6215-8

Transient synthesis of carbon-supported high-entropy alloy sulfide nanoparticles via flash Joule heating for efficient electrocatalytic hydrogen evolution

Yuntian Liao, Rongtao Zhu (✉), Wenjun Zhang, Haiyang Zhu, Yang Sun, Jiale Chen, Zhenhua Dong, and Ronghuan Lv

School of Chemical Engineering and Technology, China University of Mining and Technology, Xuzhou 221116, China

Received: 20 August 2023 / **Revised:** 15 September 2023 / **Accepted:** 20 September 2023

ABSTRACT

High entropy alloys (HEA) are frequently employed as catalysts in electrocatalytic hydrogen evolution. However, the traditional high entropy alloy synthesis methods are time-consuming, energy-intensive, and environmentally polluting, which limits their application in the hydrogen evolution reaction (HER). This study leveraged the capabilities of flash Joule heating (FJH) to synthesize carbon-supported high-entropy alloy sulfide nanoparticles (CC-S-HEA) on carbon cloth (CC) with good self-standing properties within 300 ms. The carbon thermal shock generated by the Joule heating could pyrolyze the sulfur source into gas, resulting in numerous pore structures and defects on CC, forming an S-doped carbon substrate (CC-S). Then the S atoms were used to stably anchor the metal atoms on CC-S to form high-density uniformly dispersed HEA particles. The electrochemical test results demonstrated that CC-S-HEA prepared at 60 V flash voltage had HER performance comparable to Pt/C. The density functional theory (DFT) calculation indicated that the S atoms on CC-S accelerated the electron transfer between the carbon substrate and HEA particles. Moreover, the unique electronic structure of CC-S-HEA was beneficial to H* adsorption and promoted catalytic kinetics. The simplicity and versatility of FJH synthesis are of great significance for optimizing the synthesis of HEA and improving the quality of HEA products, which provides a broad application prospect for the synthesis of nanocatalysts with efficient HER performance.

KEYWORDS

high entropy alloy, flash Joule heating, carbon thermal shock, hydrogen evolution reaction, density functional theory

1 Introduction

With the depletion of traditional fossil fuels and the escalating ecological and environmental problems, it is urgent to find renewable and environmental-friendly alternative energy sources [1–6]. As a sustainable clean energy carrier, hydrogen energy has become one of the most promising new generation energy sources [7–10]. Electrochemical catalytic water splitting is an efficient and environmentally friendly hydrogen production technology with broad application prospects [11–14]. In the cathodic hydrogen evolution reaction (HER) for electrocatalytic water splitting, electrocatalysts are crucial to accelerate the slow reaction kinetics and complex electron transfer process. Typically, noble metal-based materials such as platinum group metals are employed as HER catalysts, especially platinum-based materials, being excellent electrocatalytic materials before [15–17]. Nonetheless, their scarcity and high costs in commercial applications restrict their widespread applications. Therefore, there is a significant demand to find inexpensive non-precious metal-based catalysts with superior electrocatalytic activity as promising alternatives for HER to meet rapid development needs [18, 19]. In recent years, high entropy alloys (HEA) refer to the single-phase solid solution in which five or more metal elements arrange in a severely distorted lattice [20, 21]. Due to the diverse elemental composition and high atomic content, it provides a strong synergistic effect between various active sites, which effectively adjusts the electronic structures and adsorption-free energy of the intermediates formed on the catalysts, thereby accelerating the catalytic process, and it has been proven to be an ideal replacement for noble metal catalysts [22–24]. Shang et al. successfully prepared carbon fiber supported high-entropy Co-Zn-Cd-Cu-Mn sulfide (CoZnCdCuMnS@CF) nanoarrays via the mild cation exchange strategy [25]. Fu et al. successfully prepared a self-standing CoCrFeNiAl HEA electrocatalyst for HER by combing mechanical alloying with spark plasma sintering (SPS) consolidations [26]. Wang et al. fabricated PtNiFeCoCu HEA particles through a simple low-temperature oil phase strategy at atmospheric pressure [27].

In the realm of HEA material preparation, several traditional synthetic methods have merged in the past few years, including mechanical alloying strategies [28], melt-alloying strategies [29], sputtering deposition strategies [30], solvothermal strategies [31], etc. In summary, the traditional production processes are divided into two categories: top-down and bottom-up synthesis strategies. The former methods fabricate HEA materials by applying appropriate energy input to synthesize various bulk pure metallic materials into a single composite alloy phase [32]. While the latter

---

Address correspondence to tzhu2010@cumt.edu.cn

typically relies on chemical or physical reactions generated by the interaction of atoms or certain molecular species to prepare HEA particles [33]. However, the traditional methods of preparing HEA materials have disadvantages. For instance, in the case of the top-down synthesis strategy, the synthesized HEA materials often exhibit the disadvantages of poor substrate applicability and disordered morphological structure while demanding a substantial amount of input energy. In the case of the bottom-up synthesis strategy, the preparation process is usually time-consuming and cumbersome, requiring enormous chemical solvents and a particular working environment for the equipment. The preparation cost is relatively high while the yield of HEA is low. Therefore, there is an urgent need for a more general and controllable strategy that not only synthesizes uniformly dispersed and high-quality HEA but also achieves control over the open-pore structure that is critical for catalyst exposure and efficient mass transfer, thus significantly improving the catalyst synthesis process and catalytic performance and reducing CO_2 emissions.

This study presented the ultrafast synthesis of uniformly dispersed high entropy alloy sulfide particles (CC-S-HEA) on carbon cloth (CC) via flash Joule heating (FJH). This paper used the Joule heating generated by the internal resistance of CC to form the carbon thermal shock to anchor S atoms on CC (CC-S). The evenly distributed S atoms on CC-S anchored the multi-element metal and prevented the aggregation of HEA particles on CC at the same time, and *in situ*, carbon thermally synthesized CC-S-HEA with self-standing properties within 300 ms. In the experiment, the input energy required for synthesis was exceptionally low, which was only 302 J. Compared with traditional heating methods, Joule heating directly acted on the carbon substrate, which reduced the energy dissipation and improved the heat utilization. Additionally, the instantaneous power density and ultrafast heating/cooling rate of Joule heating (10^4–10^5 K/s) were much higher [34–40]. It is these advantages of Joule heating that are more favorable for the synthesis of nanostructures. Chen et al. utilized the ultrafast temperature-raising and cooling capabilities of Joule heating to achieve ultrafast self-assembly of reactive nanoparticles in reduced graphene oxide films [41]. Lin et al. successfully prepared high-entropy alloy nanoparticles embedded in graphene for oxygen evolution reaction (OER) by Joule heating [42]. The instantaneous carbon thermal shock improved the conductivity of CC and accelerated the transfer rate between electrons. Moreover, the gas generated by the thermal decomposition of sulfur sources and metal salts formed lots of open-pore structures on CC, which was crucial for the exposure of active sites and penetration of electrolytes for enhanced catalytic performance. The electrochemical tests showed that CC-S-HEA had comparable HER performance to Pt/C. Furthermore, combined with density functional theory (DFT) calculations, it was found that the coordination between metal atoms at different sites in CC-S-HEA provided higher electroactivity, and the incorporation of HEA particles as active sites accelerated the generation of H_2 and significantly improved the HER performance of CC. Therefore, this paper proposed the synthesis of self-standing CC-S-HEA using FJH, which proved that FJH is one of the most promising methods for the large-scale economical synthesis of HEA materials, holding valuable implications for the sustainable development of the catalytic industry.

2 Experimental

2.1 Chemicals and materials

All reagents were of analytical grade. Ethanol (C_2H_5OH), thiourea (CH_4N_2S), nickel(II) chloride hexahydrate ($NiCl_2·6H_2O$), copper(II) sulfate pentahydrate ($CuSO_4·5H_2O$), manganese(II) chloride tetrahydrate ($MnCl_2·4H_2O$), iron(III) chloride hexahydrate ($FeCl_3·6H_2O$), cobalt(II) chloride hexahydrate ($CoCl_2·6H_2O$), potassium hydroxide (KOH), and deionized water were purchased from Sinopharm Chemical Reagent Co., Ltd. (China). Acetone (C_3H_6O) was bought from Sigma-Aldrich (China). Pt/C was purchased from Macklin (China). Carbon cloth was purchased from Xinneng, Hangzhou, China).

2.2 The FJH system

The FJH system includes a control module, a charging module, a discharging module, a working module, an energy storage module, and a measurement module. In our previous work, the circuit diagram of FJH had been shown [36]. The control module includes a controller PLC and a relay; the charging module includes a charging power supply, a capacitor, a resistor, and a charging switch; the discharging module includes a capacitor, a resistor, and a discharging switch; the energy storage module is mainly composed of a capacitor; the working module includes a sample stage, a reaction box; the measurement module includes a voltage, resistance, and temperature meter. The manufacturer and model for all components are indicated in the Table S1 in the Electronic Supplementary Material (ESM).

2.3 Experimental methods

Before the experiment, CC needs to be soaked in C_3H_6O to remove impurities and washed multiple times with deionized water. Firstly, configured thiourea solution and multi-element metal salt solution: according to the concentration of 0.1 mol/L, thiourea was added into the beaker with 100 mL of absolute ethanol solution and ultrasonicated for 30 min until completing the mixing. According to the concentration of 0.1 mol/L, $CuSO_4·5H_2O$, $NiCl_2·6H_2O$, $MnCl_2·4H_2O$, $FeCl_3·6H_2O$, and $CoCl_2·6H_2O$ were sequentially added into the beaker with 100 mL of absolute ethanol and ultrasonicated for 30 min until the solution was fully well mixed.

The prepared 2 mL of thiourea solution was dropped on the CC (1 cm × 3 cm) and dried in the vacuum oven at 60 °C for 6 h. The CC was clamped on the bench and the FJH system was used to synthesize CC-S at 80 V. Then the prepared 2 mL of multi-element metal salt solution was dropped on CC-S and the CC-S was dried in a vacuum oven at 60 °C for 6 h. The CC-S was clamped on the bench and the FJH was used to synthesize CC-S-HEA at different flash voltages. FJH always worked in a vacuum environment. The samples synthesized with 20, 40, 60, and 80 V flash voltage were named CC-S-HEA_{20}, CC-S-HEA_{40}, CC-S-HEA_{60}, and CC-S-HEA_{80}. Figure S1 in the ESM showed the images of CC, CC-S, and CC-S-HEA.

2.4 Material characterization

Scanning electron microscopy (SEM) images were taken with a Zeiss Sigma 300 SEM system. A voltage of 10 keV was employed in the process of imaging. Transmission electron microscopy (TEM) was performed on a high-resolution Hitachi JEM-2100F. The molybdenum mesh support film (200 mesh) was utilized to protect the Cu signals of samples from the copper mesh support. Powder X-ray diffraction (XRD) spectra were collected with a Bruker D8 advance diffractometer using zero background sample holders at a scan rate of 2 °·min^{-1} and a 0.1° step size. X-ray photoelectron spectroscopy (XPS) data were collected using a Thermo Scientific K-Alpha scanning X-ray microprobe with a 5×10^{-9} Torr base pressure. Survey spectra were recorded using 0.5 eV step sizes with a pass energy of 140 eV. Elemental spectra were recorded using 0.1 eV step sizes with a pass energy of 50 eV. All the XPS spectra were corrected using the C 1s peaks (284.8 eV) as a reference. Raman spectra were collected by a Horiba Raman microscope outfitted with a 532 nm laser. Brunauer–Emmett–Teller (BET) surface area analysis was conducted with a Micromeritics APSP2640 BET surface analyzer, with nitrogen as the analysis gas. Samples were degassed for 8 h at 200 °C under a high vacuum before analysis.

2.5 Electrochemical measurements

The HER test was conducted by a CHI604E electrochemistry workstation with a typical three-electrode cell in 1 M KOH electrolyte. The samples, Hg/HgO electrode, and platinum plate acted as working electrodes, reference electrodes, and counter electrodes, respectively. Before testing, the solution was continuously purged with high-purity nitrogen for 30 min to remove oxygen. Linear sweep voltammetry (LSV) curves were measured in 1 M KOH alkaline media at a 5 $\mathrm{mV \cdot s^{-1}}$ scan rate. Cyclic voltammogram (CV) curves were obtained at the scan rate of 20, 40, 60, 80, 100, and 120 $\mathrm{mV \cdot s^{-1}}$, respectively. The double-layer capacitance (C_{dl}) was collected by CV measurements with various scan rates as a function. Electrochemical impedance spectroscopy (EIS) was measured in the frequency range from 100,000 to 0.1 Hz at an overpotential of 300 mV. At a scanning speed of 5 $\mathrm{mV \cdot s^{-1}}$, the electrode material was subjected to 1000 cyclic voltammetry tests in an alkaline environment of 1 M KOH electrolyte to test the stability of the catalyst. All potentials were converted to reversible hydrogen electrode (RHE) voltages ($E_{\mathrm{RHE}} = E_{\mathrm{Hg/HgO}} + 0.098 + 0.059 \times \mathrm{pH}$).

2.6 Flash Joule heating process simulation

The structure of the flash Joule heating process was set as follows: the width, length, and thickness of CC: 10, 50, and 1 mm; the width, length, and thickness of the copper electrode: 10, 14, and 1 mm. The finite element analysis was conducted based on electromagnetic thermophysical field simulations. The upper surface of the left copper electrode was set as the charging voltage surface, and the lower surface of the right copper electrode was used for the ground. Table S2 in the ESM displays the relevant properties of specific materials.

Since the current passed through the samples when the FJH was working, Joule heating was generated *in situ* due to the existing internal resistance, and the samples generated heat instantaneously. This process involved the multi-physical coupling of electromagnetic heat. The finite element simulation first used the current physical field, and set the left and right sides of the copper electrode as the discharge voltage plane and the ground plane respectively. Then used the physics of heat transfer in solids, set the external temperature to 293.15 K, and selected the convective heat flux type.

In the case of electromagnetic-thermal multiphysics coupling, the assumed equations used are as follows

$$\rho C_{\mathrm{p}} \frac{\partial T}{\partial t} + \rho C_{\mathrm{p}} u \cdot \nabla T = \nabla \cdot (k \nabla T) + Q_{\mathrm{e}} \tag{1}$$

where ρ is the density of the material, C_{p} is the heat capacity of the material at constant pressure, T is the temperature of the material, t is the FJH synthesis time, u is the displacement field vector of the material, Q_{e} is the heat generated under the action of Joule heating, k is the thermal conductivity.

2.7 Calculation methods

DFT simulations were run with the Cambridge Sequential Total Energy Package (CASTEP), one of the main modules in the Materials Studio program. The generalized gradient approximation of Perdew-Burke-Ernzerhof exchange-correlation functionals was adopted for all the calculations. Valence electrons were described by the Kohn–Sham wave functions expanded in a plane wave basis with an energy cutoff set to 400 eV. The ultrasoft pseudopotentials with the Broyden-Fletcher-Goldfarb-Shannon (BFGS) algorithm were chosen for related ground state geometry optimizations. The reciprocal space was sampled using a 2 × 2 × 1 Monkhorst-Pack grid. The periodic boundary condition (PBC) was set to maintain a 15 Å vacuum region above the surface to avoid attractions from adjacent periodic mirror images. The Gibbs free energies for hydrogen adsorption ($\Delta G_{\mathrm{H^*}}$) were calculated from the equation: $\Delta G_{\mathrm{H^*}} = \Delta E_{\mathrm{H^*}} + \Delta \mathrm{ZPE} - T\Delta S$, where $\Delta E_{\mathrm{H^*}}$, ΔZPE, T, and ΔS represent the binding energy, zero-point energy change, temperature, and entropy change of the $\mathrm{H_{ad}}$ adsorption system, respectively.

3 Results and discussion

3.1 Character of flash Joule heating process

CC is a well-supported carbon source that has good electrical conductivity. Therefore, CC is suitable as a substrate for FJH synthesis of high-efficiency HEA catalysts. The carbon substrate was directly impregnated with thiourea and multi-element metal salt solution and dried to obtain a carbon-based precursor. Based on not requiring any chemical gases, FJH generates Joule heating *in situ* on CC ultra-fast and synthesizes CC-S and CC-S-HEA

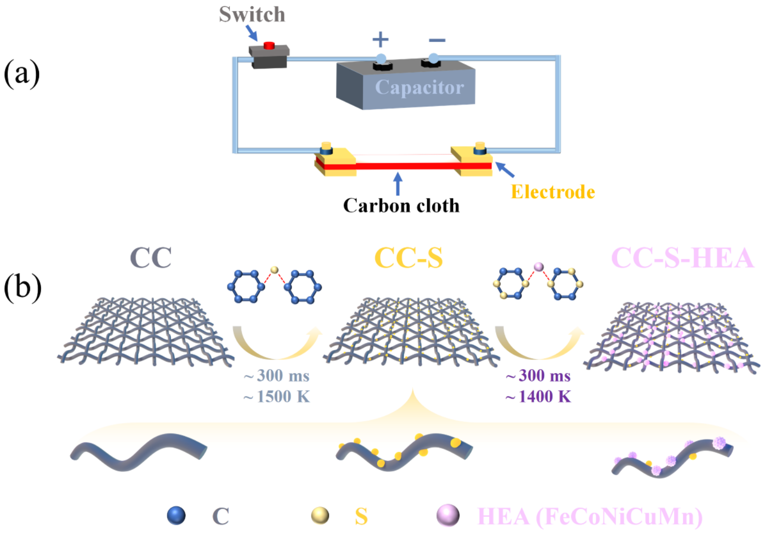

Figure 1 (a) Schematic diagram of FJH system. (b) Schematic diagram of the synthesis mechanism of CC-S and CC-S-HEA by FJH.

successively *in situ*. The FJH system is shown in Fig. 1(a). The two ends of CC were clamped on the copper sheet respectively, the capacitor in FJH would discharge CC instantaneously, and the synthesis temperature on CC was regulated by controlling the flash voltage. The schematic diagram of the synthesis process of CC-S-HEA by FJH is shown in Fig. 1(b). During the synthesis of FJH, the thermal shock of carbon produced by CC under the action of Joule heating caused the pyrolysis of thiourea instantaneously, in which the S atoms reacted with the carbon atoms on CC, not only doping the S atoms in the CC but also forming abundant defect sites on the CC surface. Then the metal salt solution rich in five metal ions (Fe^{3+}, Co^{2+}, Ni^{2+}, Cu^{2+}, and Mn^{2+}) was dropped on CC-S. When the flash voltage was 60 V, CC-S heated up to 1400 K within 300 ms. The CC-S-HEA was synthesized due to the abundant open-pore structures and abundant surface defects on CC-S as well as S atoms serving as the anchor site for efficient dispersion and high surface coverage of HEA.

The carbon skeleton of CC was not destroyed due to the extremely short synthesis time. As shown in Fig. 2(a), CC-S-HEA

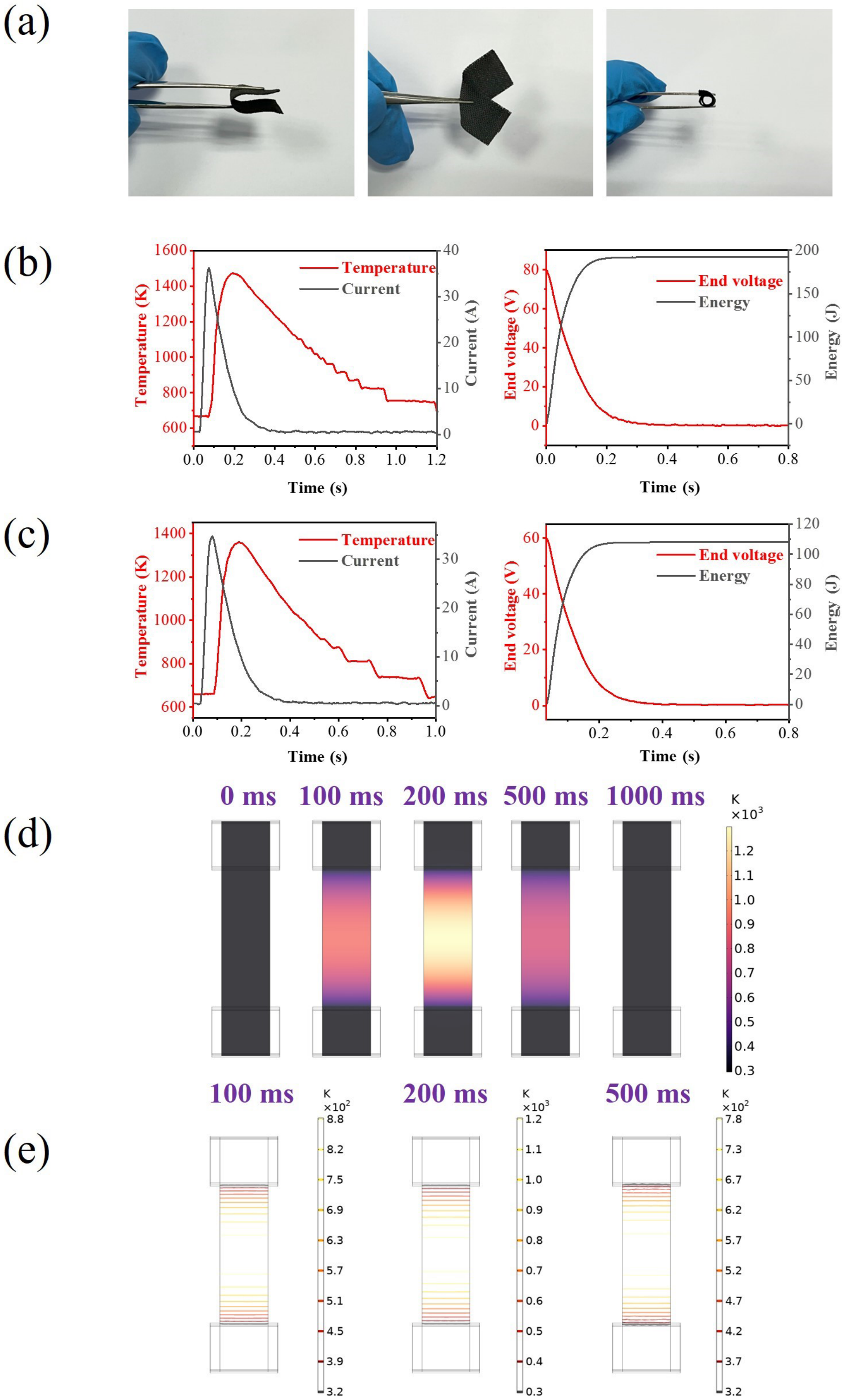

Figure 2 (a) CC-S-HEA with good self-standing. (b) and (c) Electrical signal and energy change when synthesizing CC-S and CC-S-HEA. (d) and (e) Simulated the temperature and temperature field change of the synthesized CC-S-HEA (to better display the temperature and temperature field change of the samples, the copper electrode is not shown).

maintained good self-standing. Moreover, the exceptionally high synthesis temperature increased the degree of graphitization of CC and thus increased the conductivity of CC. As shown in Fig. S2 in the ESM, the resistivity of CC gradually decreased with the process of FJH. When FJH synthesized CC-S, a pulse current lasting 300 ms was generated on CC. The surface temperature of CC was also instantly increased to 1500 K, and the energy required for synthesis was only 192 J calculated by Eq. (2) (Fig. 2(b)). When synthesizing CC-S-HEA, the temperature of CC-S rose to 1400 K within 300 ms and cooled down to room temperature within 1 s, and the energy required for synthesis was 110 J (Fig. 2(c)). The results showed that compared with the traditional catalyst synthesis methods, the instantaneous current generated by FJH made the carbon substrate heat up instantly (10^5 K·s^{-1}) under the action of Joule heating, and the cooling rate (10^4 K·s^{-1}) was extremely fast, requiring only a very low enter energy. To better optimize the synthesis parameters of CC-S-HEA and verify whether the Joule heating generated by the FJH synthesis process is uniform, COMSOL software was used to conduct a finite element analysis on the FJH synthesis process. In Fig. 2(d), the temperature at the center of CC was the highest, and the closer it was to the electrode, the lower the sample temperature became, indicating that the energy output by the FJH was consumed on the CC. As shown in Fig. 2(e), by studying the distribution of the temperature field, it verified whether the Joule heating generated within CC was uniformly distributed when the FJH was working, proving that the distribution of Joule heating generated on CC was very uniform and the material on the CC was reacted fully. To verify the results of the simulation, the high-speed camera was used to record the FJH synthesis process (Fig. S3 in the ESM). When the current passed through the CC, the temperature of the CC rose and a uniform red light was generated on the surface, which proved that the generated Joule heating was evenly distributed, and then a dazzling light spot was produced on the entire samples at about 180 ms. Finally, the intensity of the light spot gradually weakened as the temperature of CC decreased within 1 s, as also supported by the simulated results.

$$E = (V_1^2 - V_2^2) \times C/2 \tag{2}$$

where E denotes the energy of the capacitor discharge; V_1 represents the initial voltage; V_2 is the final voltage; C denotes the capacitance capacity.

To explore the process of ultrafast synthesis of CC-S-HEA by FJH, the study theoretically analyzed the feasibility of the synthesis process. During the synthesis process, the input energy of FJH directly acted on the carbon substrate, being absorbed and dissipated by Joule heating. The energy change followed the law of energy conservation, as shown in Eqs. (3)–(5)

$$E_{\text{input}} = E_{absorb} + E_{\text{dissipate}} = P_{\text{FJH}} \cdot t_{\text{FJH}} \tag{3}$$

$$E_{\text{absorb}} = \xi \cdot E_{\text{input}} \tag{4}$$

$$E_{\text{absorb}} = \xi \cdot P_{\text{FJH}} \cdot t_{\text{FJH}} \tag{5}$$

where E_{input} is the total energy stored by FJH; E_{absorb} represents the energy absorbed by the carbon substrate, where the absorbed energy is converted into thermal energy when Joule heating is generated; $E_{\text{dissipate}}$ is the dissipated energy that does not participate in the process of generating Joule heating. Since FJH directly acts on the carbon substrate, the conversion between E_{input} and E_{absorb} has a coefficient relationship due to the influence of the working environment, and ξ is the energy conversion coefficient.

Combining Eqs. (3)–(5) yields Eq. (6)

$$E_{\text{absorb}} = \xi \cdot P_{\text{FJH}} \cdot t_{\text{FJH}} = Q \tag{6}$$

$$Q = c \cdot m \cdot (\Delta T) \tag{7}$$

$$K = \frac{\Delta T}{t_{\text{FJH}}} = \frac{\xi \cdot P_{\text{FJH}}}{c \cdot m} \tag{8}$$

Q refers to the heat energy generated on the carbon substrate; K is the rate of Joule heating on the carbon substrate; c and m denote the specific heat capacity and mass of materials, respectively. As shown in Eqs. (7) and (8), when the natural features of a material are excluded, the heating rate is the coupling of power (P_{FJH}) and time (t_{FJH}). Compared with traditional heating methods, FJH produces an extremely fast heating rate under the same energy input in an extremely short time, instantly making the carbon substrate reach an extremely high reaction temperature.

In chemical thermodynamics, the Arrhenius equation is used to assess the relationship between the chemical reaction rate and temperature in the FJH process [43], as shown in the following equation

$$k = A \cdot \mathrm{e}^{\frac{-E_a}{RT}} \tag{9}$$

where k refers to the chemical reaction rate on the material; R is the molar gas constant; T is the FJH reaction temperature; E_a is the activation energy of the material; A is the Arrhenius constant. According to Eq. (9), the higher the reaction temperature, the faster the chemical reaction rate of the material, proving that FJH instantly makes the carbon substrate reach an extremely high temperature, which speeds up the chemical reaction rate on the carbon substrate so that CC-S-HEA is synthesized at an ultra-fast speed.

3.2 Influence of flash Joule heating on the microstructure of CC-S-HEA

Microstructural changes in CC were observed using SEM. In Fig. 3(a), the surface of untreated CC was very smooth with almost no pores. As shown in Fig. 3(b), S particles with high coverage and extremely small size were observed on the surface of CC-S. The energy dispersive spectroscopy (EDS) image reflected that the arrangement of S particles on the CC surface was very uniform

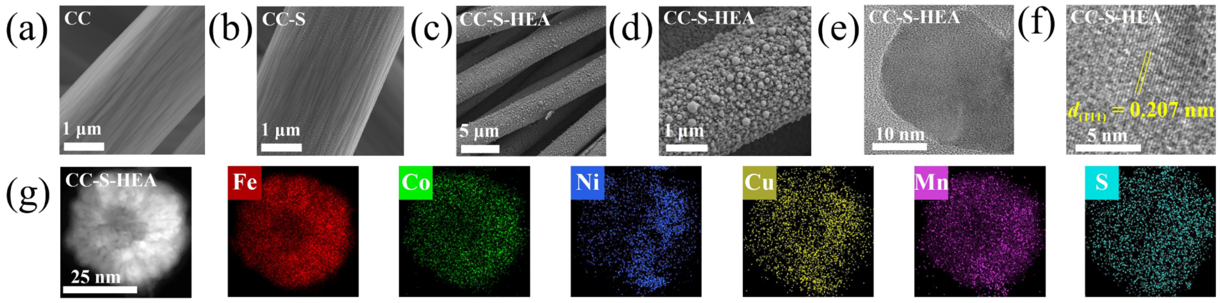

Figure 3 Microstructural changes of samples after FJH treatment. SEM images of (a) CC, (b) CC-S, and (c) and (d) CC-S-HEA. (e) TEM, (f) HRTEM, and (g) EDS mapping images of CC-S-HEA synthesized by FJH.

(Fig. S4 in the ESM), indicating that S atoms were successfully loaded on CC-S, the uniform distribution of high-density S particles was crucial to ensure the formation of high-density uniformly dispersed HEA particles and the stability of the formed S-HEA bonds. And the sulfur source was pyrolyzed under the action of Joule heating, and the strong gas produced many tiny pores on the surface of CC, which provided more active sites for subsequent reactions. As shown in Figs. 3(c) and 3(d), due to the high loading and uniformly dispersed S particles on CC-S and the large number of defects on the surface, which well anchored the metal atoms and the multi-element metal salts reacted with CC-S to successfully synthesize CC-S-HEA under the ultrafast carbon thermal shock. The particle size of HEA was extremely small, which significantly improved the specific surface area. In Fig. S5 in the ESM, the EDS energy spectrum showed that CC-S-HEA treated with FJH still had a high S retention rate, and it was observed that HEA particles were uniformly and densely dispersed in the CC-S surface. TEM measurements were conducted to characterize the nanostructure of the prepared samples. Figure 3(e) showed TEM images of very small CC-S-HEA nanoparticles. Figures 3(f) and 3(g) show the high-resolution TEM (HRTEM) and EDS mapping images of CC-S-HEA, which not only proved that CC-S-HEA is an alloy solid solution structure but also that the interplanar crystal spacing (111) was 0.207 nm. Moreover, the various elements in CC-S-HEA were evenly distributed.

To verify the anchoring effect of S atoms on metal atoms prevented the agglomeration of HEA, this experiment compared CC-HEA (Fig. S6 in the ESM). The metal salt solution was directly dropped on the CC without S and treated by FJH to synthesize CC-HEA. The result showed that the metal atoms aggregated due to free movement on CC under the action of Joule heating, and since there were almost no defects on the untreated CC, the loading of HEA was less compared to that of CC-S-HEA. This evidence indicated that S atoms loading on CC and the ultrafast carbon-thermal shock were crucial for the synthesis of high-coverage, high-stability HEA. In order to judge the structural stability of CC-S-HEA. As shown in Fig. S7 in the ESM, after the HER performance test and cycle stability test, CC-S-HEA still maintained the original nanostructure. There was no aggregation or shedding of particles, proving that the CC-S-HEA synthesized by FJH had a stable structure.

Gibbs free energy is often used in chemical thermodynamics to determine whether a chemical reaction will occur under the same working environment [44], and ΔG is called Gibbs free energy change, as shown in the following equation

$$\Delta G = \Delta H - T\Delta S \tag{10}$$

where ΔH refers to the enthalpy of the material, T is the reaction temperature, and ΔS is the mixing entropy of the material. As shown in Eq. (10), the higher reaction temperature leads to lower ΔG. When $\Delta G < 0$, it demonstrates that the chemical reaction occurs. Compared with the traditional HEA synthesis methods, the ultra-fast carbon thermal shock of FJH makes the carbon substrate reach an extremely high temperature *in situ* quickly. Therefore, the solid solution HEA was easily formed during this process, which was also consistent with the observed CC-S-HEA.

3.3 Influence of flash Joule heating on the chemical composition of CC-S-HEA

In order to confirm further the successful synthesis of the CC-S-HEA, the crystal structure was studied by XRD. In Fig. 4(a), compared with untreated CC, the two main peaks of CC-S-HEA appeared at about 44° and 51° in 2θ, which were related to its (111) and (200) crystal planes, respectively, and it was determined that CC-S-HEA is a single-phase structure of fcc phase. The XRD spectrum of CC-S-HEA that had undergone the HER performance test and the stability test was shown in Fig. S8 in the ESM. Even after long-term electrochemical testing, CC-S-HEA can still maintain a stable single-phase solid solution structure,

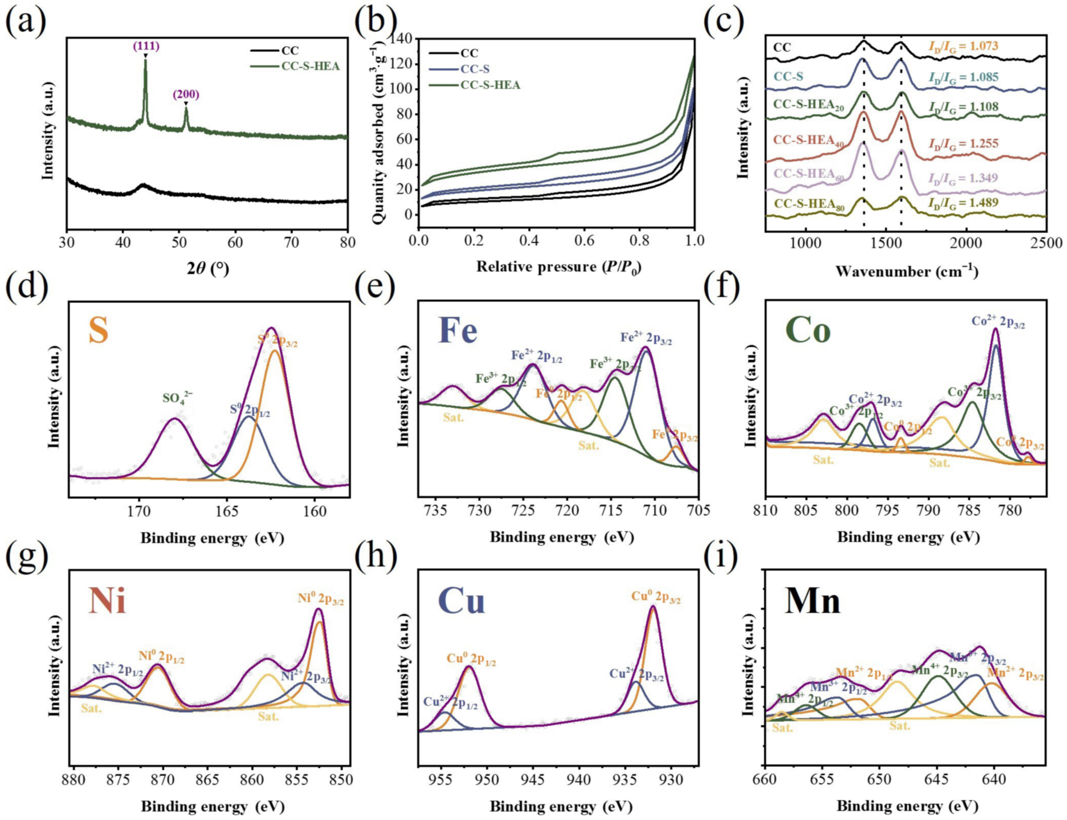

Figure 4 (a) XRD spectra of CC and CC-S-HEA. (b) N_2 adsorption–desorption curves of CC, CC-S and CC-S-HEA. (c) Raman spectra of CC, CC-S and CC-S-HEA. (d)–(i) High-resolution XPS spectra of different elements.

proving that CC-S-HEA had a stable chemical structure.

The effect of carbon thermal shock generated by Joule heating on the CC pore structures was further observed by BET. In Fig. 4(b), the surface area of CC without any treatment was 37.15 $m^2 \cdot g^{-1}$. The sulfur sources and metal salts were pyrolyzed under the Joule heating to generate gas, which impacted the surface of CC to form pores. The specific surface areas of CC-S and CC-S-HEA gradually increased to 67.43 and 113.67 $m^2 \cdot g^{-1}$, and a typical type IV nitrogen adsorption–desorption isotherm with an obvious hysteresis loop at a relative pressure (P/P_0) from 0.45 to 0.99 was observed in the case of CC-S-HEA, which indicated that micro- and mesopores existed in CC-S-HEA [45]. The specific surface area of CC gradually increased during the synthesis of FJH, indicating that under the action of Joule heating, the instantaneous carbon thermal shock and the gas generated by the pyrolysis of the loaded material gradually increased the open-pore structures of CC, which was more conducive to the exposure of HEA particles and penetration of electrolyte.

To explore the influence of the defects on the CC surface during the synthesis of FJH, the change of the defect degree on the CC surface was assessed by comparing the Raman characteristic peaks of different samples (Fig. 4(c)). The D peak and G peak are related to the defect and atomic hybridization mode of the material, respectively. The peak intensity ratio I_D/I_G of the D peak and the G peak is commonly used to characterize the surface defect degree of the material [46]. The larger the I_D/I_G value, the higher the surface defect degree of the corresponding material. With the progress of FJH, the I_D/I_G gradually increased from CC to CC-S-HEA, and with the increase of flash voltage, the I_D/I_G of CC-S-HEA also gradually increased. When the flash voltage increased, the carbon thermal shock generated, and the gas generated by the pyrolysis of the load were stronger, which effectively formed defects on the surface of CC. It further proved that the carbon thermal shock generated by Joule heating and the gas generated by the pyrolysis of the load increases the defect degree of the CC surface, and the higher the synthesis temperature, the higher the defect degree of the CC surface.

XPS was used to explore the chemical state of CC-S-HEA. In the high-resolution XPS spectrum of S (Fig. 4(d)), the peaks at 162.3 and 163.8 eV belonged to S^0 $2p_{3/2}$ and S^0 $2p_{1/2}$, respectively; the peaks at 168.0 eV belonged to SO_4^{2-}. The high-resolution XPS spectrum of Fe is shown in Fig. 4(e), the peaks at 707.7 and 720.7 eV belonged to Fe^0 $2p_{3/2}$ and Fe^0 $2p_{1/2}$, respectively; the peaks at 711.1 and 723.9 eV correspond to Fe^{2+} $2p_{3/2}$ and Fe^{2+} $2p_{1/2}$, respectively; the peaks at 714.5 and 727.6 eV correspond to Fe^{3+} $2p_{3/2}$ and Fe^{3+} $2p_{1/2}$, respectively; the peaks at 718.9 and 733.1 eV were two satellite peaks of Fe [47]. The high-resolution XPS spectrum of Co was shown in Fig. 4(f), the peaks at 777.8 and 793.4 eV correspond to Co^0 $2p_{3/2}$ and Co^0 $2p_{1/2}$, respectively; the peaks at 781.8 and 796.9 eV belonged to Co^{2+} $2p_{3/2}$ and Co^{2+} $2p_{1/2}$, respectively; the peaks at 784.7 and 798.5 eV belonged to Co^{3+} $2p_{3/2}$ and Co^{3+} $2p_{1/2}$, respectively; the peaks at 788.4 and 802.9 eV were two satellite peaks of Co [48]. The high-resolution XPS spectrum of Ni was shown in Fig. 4(g), the peaks at 852.6 and 870.5 eV belonged to Ni^0 $2p_{3/2}$ and Ni^0 $2p_{1/2}$, respectively; the peaks at 854.3 and 875.5 eV belonged to Ni^{2+} $2p_{3/2}$ and Ni^{2+} $2p_{1/2}$, respectively; the peaks at 858.2 and 877.8 eV were two satellite peaks of Ni [26]. The high-resolution XPS spectrum of Cu was shown in Fig. 4(h), the peaks at 932.1 and 952.0 eV correspond to Cu^0 $2p_{3/2}$ and Cu^0 $2p_{1/2}$, respectively; the peaks at 933.8 and 954.7 eV belonged to Cu^{2+} $2p_{3/2}$ and Cu^{2+} $2p_{1/2}$, respectively [49]. The high-resolution XPS spectrum of Mn was shown in Fig. 4(i), the peaks at 640.2 and 651.9 eV correspond to Mn^{2+} $2p_{3/2}$ and Mn^{2+} $2p_{1/2}$, respectively; the peaks at 641.7 and 653.9 eV correspond to Mn^{3+} $2p_{3/2}$ and Mn^{3+} $2p_{1/2}$, respectively; the peaks at 644.9 and 656.5 eV correspond to Mn^{4+} $2p_{3/2}$ and Mn^{4+} $2p_{1/2}$, respectively. The peaks at 648.5 and 658.6 eV were two satellite peaks of Mn [50]. The high-resolution XPS spectra of the five metal elements of CC-HEA were shown in Fig. S9 in the ESM. By comparing the high-resolution XPS spectra of CC-S-HEA and CC-HEA, it was found that the peak position of metallic Fe^0 2p shifted to higher binding energy (~ 0.2 eV) in CC-S-HEA, indicating that some electrons were transferred from Fe to S. Comparing the high-resolution XPS spectra of other metal elements, it was found that the positions of the metal peaks shifted to higher binding energies, indicating that S atoms doped in CC-S interacted with metal atoms, leading to the formation of S-HEA bonds, which effectively controlled the electronic structure of CC-S-HEA. The metal-substrate interaction and electron transfer were further verified by charge density distribution calculations of HEA on CC and on CC-S (Fig. S10 in the ESM). Compared with CC, more electrons were transferred from HEA to CC-S substrate, proving that more electrons transfer between HEA and CC-S is possible.

3.4 Electrochemical characterization of samples

The catalytic activities of the CC-S-HEA composites were evaluated by LSV measurements in 1 M KOH electrolyte using a standard three-electrode system. Figure 5(a) shows the LSV curves of S-HEA_{20}, S-HEA_{40}, S-HEA_{60}, S-HEA_{80}, and Pt/C. When the current density reached 10 $mA \cdot cm^{-2}$, the overpotential of Pt/C was only 97 mV, and that of CC was 310 mV. After FJH treatment, the overpotentials of CC-S-HEA_{20} and CC-S-HEA_{80} were 190 and 248 mV, respectively. The overpotentials of CC-S-HEA_{40} and CC-S-HEA_{60} were 130 and 115 mV, respectively. The overpotential of CC-S-HEA was notably reduced compared to that of CC. As the HEA in CC-S-HEA provided many active sites, the pore structures and defects were conducive to the exposure of active sites and the penetration of electrolytes, which accelerated the transmission between electrons and exceptionally improved the HER performance. In addition, the overpotential of CC-S-HEA_{60} was relatively low. When the current density reached 50 $mA \cdot cm^{-2}$, the required potential energy of CC-S-HEA_{60} was even smaller. In contrast, CC-S-HEA_{60} was closer to the overpotential of Pt/C. This is because the flash voltage of FJH was directly proportional to the synthesis temperature. Insufficient flash voltage hinders the complete reaction of metal ions and atoms on CC-S, resulting in inadequate HEA loading. Conversely, the carbon thermal shock generated by excessively high flash voltage makes some of the formed HEA on CC-S unstable or even decompose, which was not conducive to the catalytic activity of CC-S-HEA. Therefore CC-S-HEA_{60} had better catalytic activity. Tafel slopes derived from LSV curves were calculated to investigate the mechanism of HER activity [51]. As shown in Fig. 5(b), the Tafel slope of Pt/C was 88.8 $mV \cdot dec^{-1}$. The Tafel slopes corresponding to CC, CC-S-HEA_{20}, CC-S-HEA_{40}, CC-S-HEA_{60}, and CC-S-HEA_{80} are 268.1, 187.6, 161.2, 94.2 and 214.2 $mV \cdot dec^{-1}$, respectively. CC-S-HEA_{60} had the smallest Tafel slope, indicating that its hydrogen evolution rate was the fastest [52] and it was an excellent hydrogen evolution catalyst.

To further understand the interface reactions and electrode kinetics in the HER process, the EIS analysis of the CC-S-HEA catalysts was conducted in the same three-electrode system [52]. The combined circuit of R_{ct} in parallel with CPE and series with R_s was used to simulate the EIS results (Fig. 5(c)). CC had the largest semicircle radius, while CC-S-HEA_{60} presented a more regular semicircle with the smallest radius in the high-frequency region. As calculated by simulation, the R_{ct} corresponding to CC-S-HEA_{20}, CC-S-HEA_{40}, and CC-S-HEA_{80} were 19, 12, and 15 Ω, respectively. CC-S-HEA_{60} had the lowest R_{ct} of 9.5 Ω, while the impedance of CC was as high as 300 Ω. After FJH treatment, the

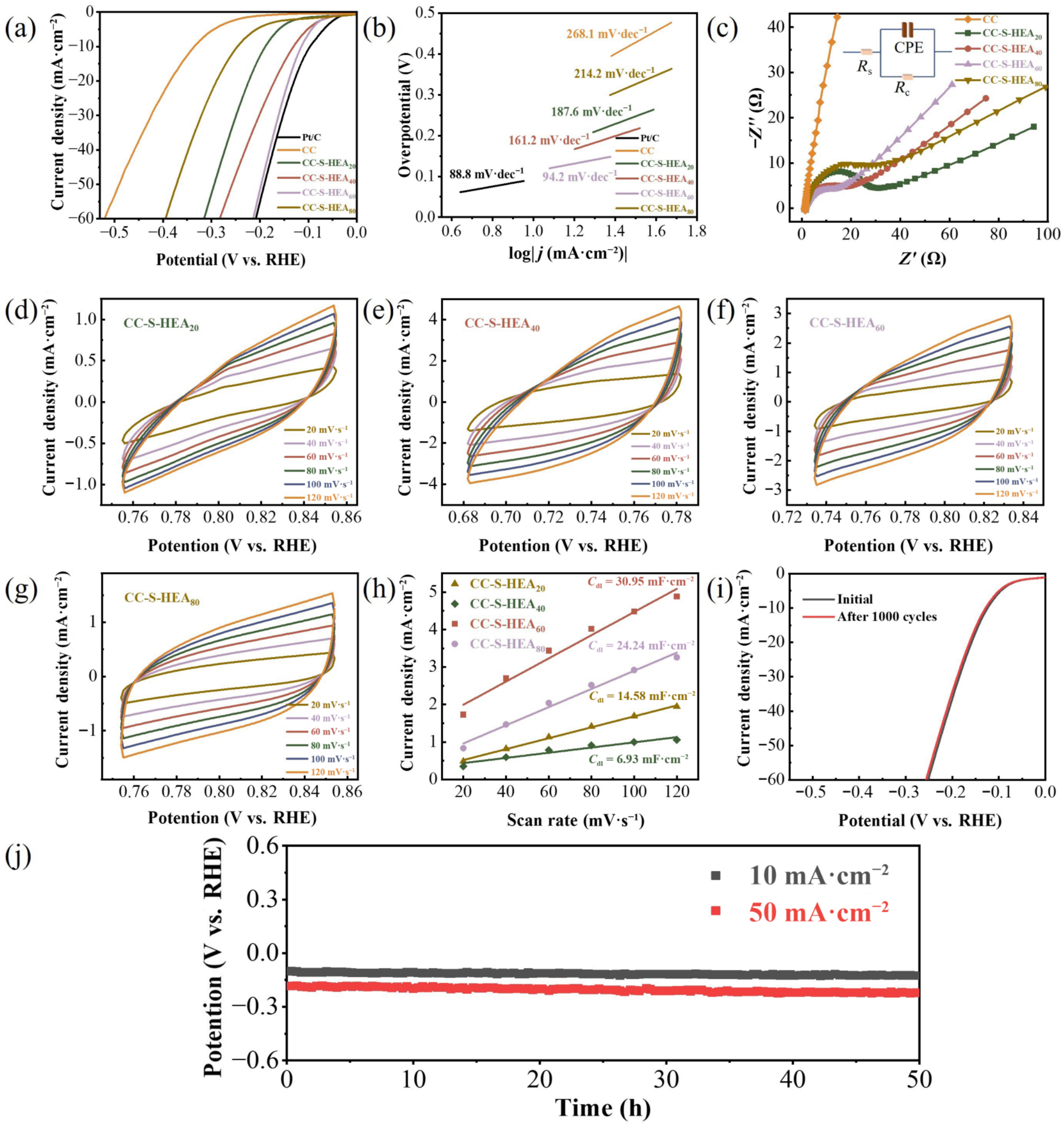

Figure 5 (a) LSV curves of different catalysts. (b) Tafel slopes of different catalysts. (c) EIS spectra of different catalysts. (d)–(g) CV curves of CC-S-HEA$_{20-80}$. (h) ECSA diagrams of CC-S-HEA$_{20}$, CC-S-HEA$_{40}$, CC-S-HEA$_{60}$, and CC-S-HEA$_{20}$. (i) The comparison of the 1st and 1000th LSV curve for CC-S-HEA$_{60}$. (j) Chronopotentiometry curves of CC-S-HEA in 1M KOH solution at different current densities.

impedance of CC-S-HEA was notably reduced because the carbon thermal shock generated by Joule heating in the FJH process improved the degree of graphitization of CC, making CC-S-HEA have good electrical conductivity. When the CC-S-HEA was used as the working electrode to exchange charges with the electrolyte on the contact surface, the free electrons were less hindered and transferred at a relatively high speed, which made the CC-S-HEA have better electrochemical activity [53]. Since CC-S-HEA$_{60}$ had the smallest impedance and the fastest charge transfer rate during catalysis, it exhibited the most excellent HER catalytic performance.

Usually, the electrochemical double-layer capacitance (C_{dl}) was linearly proportional to electrochemical active surface area (ECSA). To calculate the C_{dl} of the CC-S-HEA catalyst, a CV test was conducted on the material at various scan rates [54]. As shown in Figs. 5(d)–5(g), the CV curves of CC-S-HEA synthesized with different flash voltages maintained a good rectangular shape, which proved that the high-density and uniformly distributed HEA particles were stably wrapped in CC-S, so that CC-S-HEA had stable electrochemical performance. The electrochemically active areas of CC-S-HEA at different scanning speeds were calculated by CV curves (Fig. 5(h)). The C_{dl} values of CC-S-HEA$_{20}$, CC-S-HEA$_{40}$, CC-S-HEA$_{60}$, and CC-S-HEA$_{80}$ were 14.58, 6.93, 30.95, and 24.24 mF·cm^{-2}, respectively, proving that CC-S-HEA$_{60}$ had the largest ECSA and good electrocatalytic activity.

The stability of catalytic materials is another important indicator for evaluating HER performance. Figure 5(i) showed the comparison of the 1st and 1000th polarization curves of the CC-S-HEA$_{60}$, and its scanning speed was 5 mV·s^{-1}, which observed that the 1st and 1000th polarization curves coincided, and the overpotential difference required to achieve the same current density was only about 5 mV. This is because the excellent self-standing property of CC-S-HEA provided a stable skeleton structure and the stability of HEA, CC-S-HEA$_{60}$ still maintained good catalytic activity after 1000 LSV tests and had excellent catalytic stability. The HER stability of CC-S-HEA was tested using the chronopotentiometry technique. Figure 5(j) showed the chronopotentiometry curves of CC-S-HEA at a current density of 10 and 50 mA·cm^{-2}. It showed that CC-S-HEA with a special stable structure displayed the long-term electrochemical stability without obvious potential shift.

3.5 DFT theoretical calculation

To reveal the synergistic effect of HEA particles on enhancing the catalytic activity of HER on the CC-S substrate, CC, CC-S, and CC-

S-HEA models were established (Fig. S11 in the ESM), and DFT calculations were carried out to identify the roles of individual metal sites and their synergistic effects. The total density of states (TDOS) and the projected density of states (PDOS) showed the electronic structure of different materials [55, 56]. For the electrocatalysts, high electrical conductivity was essential for the efficient reaction processes. As shown in Fig. 6(a), the calculated TDOS of the CC-S-HEA was not 0 at Femi level (E_F), demonstrating the metallic nature of the HEA samples with faster electron migration and conductance rate [57]. In addition, the PDOS of each metal component in the CC-S-HEA model was shown in Fig. S12 in the ESM. The d-band center of Cu was far from the E_F, proving that the Cu sites had electron-rich properties and acted as the electron reservoir for HER. At the same time, the 3d orbitals of Mn and Fe had a wide band structure, enabling fast electron transfer. The Ni and Co sites, taking up adjacent positions near E_F, demonstrated high electroactivity, which helped to stabilize the vital intermediate (H*) produced during the alkaline HER process by adsorbing water dissociation (the Volmer step) [57]. The study also analyzed the variation of PDOS of different metal atoms on the bottom layer and surface of HEA to understand their role in enhancing HER activity (Figs. 6(b)–6(f)). When these metal sites moved from the bottom layer to the surface, the d-band center of the metal atoms except Mn gradually approached E_F, which indicated that these metal atoms on the surface not only enhanced the adsorption of the intermediate (H*) but also enhanced the electron transfer efficiency, which was conducive to improving the electron transfer between metal atoms. Mn sites displayed the site-independent electronic structure from the interior to the surface, which helps maintain the stable adsorption of intermediates and initial electroactive features [27].

The hydrogen absorption Gibbs free energy (ΔG_{H^*}) was used as a major evaluation criterion for HER performance [58]. The closer ΔG_{H^*} was to 0, the more likely the adsorbed H* on the Heyrovsky step be desorbed to produce H_2 [59]. The model of adsorbing H* on different catalysts was shown in Fig. 6(g), and it was calculated that CC exhibited the largest ΔG_{H^*} (2.53 eV) (Fig. 6(h)), proving that it was difficult to desorb H* on CC. But the ΔG_{H^*} of adsorbing H* on the S sites of CC-S was smaller than that of CC, proving that incorporating S atoms is beneficial to improve the HER performance. To compare the HER performance of CC-S-HEA, this paper established the Pt (111) model as shown in Fig. S13 in the ESM, and the calculated ΔG_{H^*} of Pt (111) was −0.09 eV, the ΔG_{H^*} of CC-S-HEA was −0.14 eV, proving that our established CC-S-HEA has comparable HER performance to Pt (111), which was consistent with our experimental results. These DFT calculation results demonstrated that the metallic nature of CC-S-HEA, which had faster electron migration and conductivity, and the synergistic effect between different metal sites could make CC-S-HEA maintain high electrical activity, and CC-S-HEA had comparable HER performance to Pt (111), which was significantly improved compared to CC, also inconsistent with the electrochemical experiment results.

4 Conclusions

In this study, CC was used as the carbon substrate. During the FJH process, S atoms were first anchored on CC to form the CC-S substrate, and then CC-S-HEA with high-density and uniformly distributed HEA particles were successfully synthesized using the anchoring effect of S on metal atoms. CC-S-HEA maintained a good self-supporting property and required a very short synthesis time (~ 300 ms), and the energy required for the reaction was only

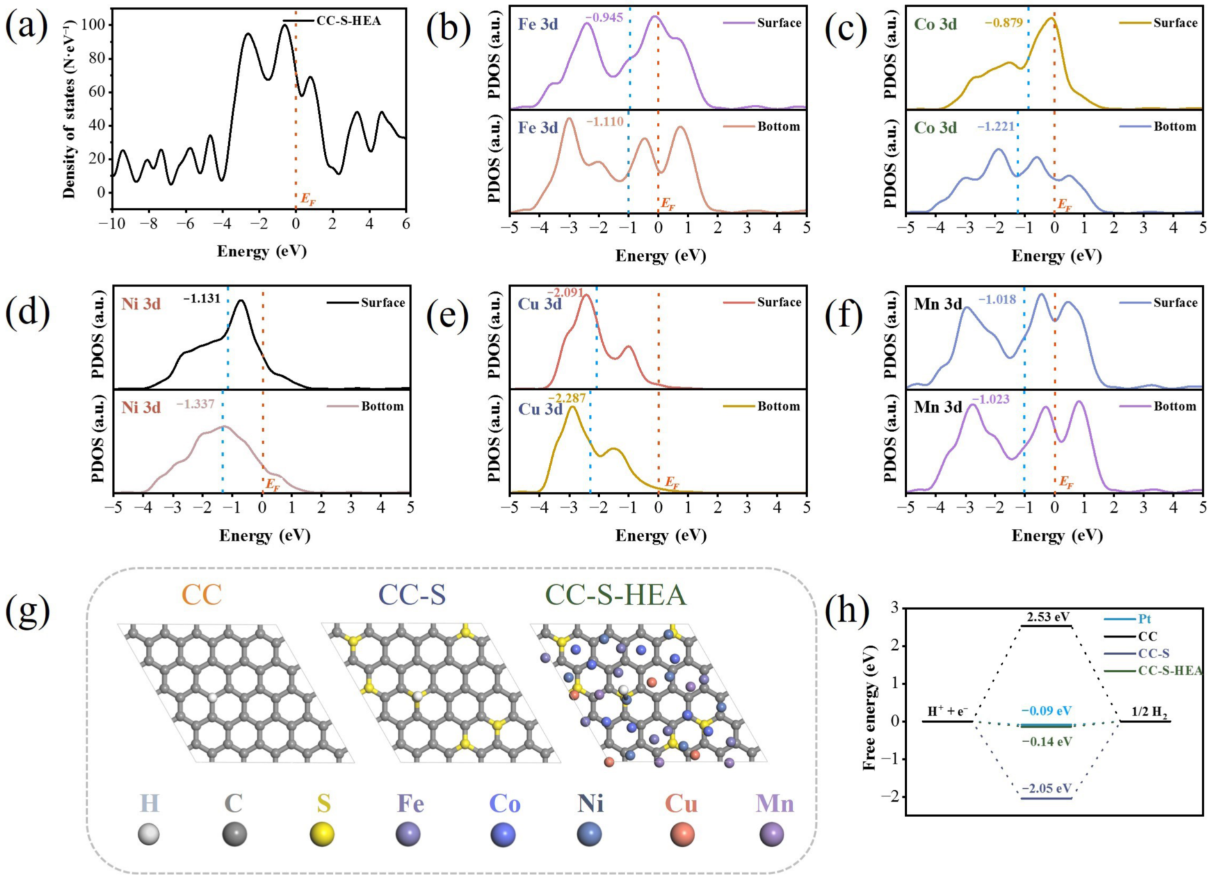

Figure 6 (a) TDOS curve of CC-S-HEA. (b)–(f) PDOS curves of Fe, Co, Ni, Cu, and Mn at different sites on the surface and bottom of CC-S-HEA (the position of the blue straight line represents the d-band center of the atom, and the position of the red straight line represents EF). (g) Adsorption sites of different catalysts for H*. (h) Gibbs free energy profiles calculated by DFT for different catalysts.

about 302 J. The finite element analysis of the FJH synthesis process was carried out, and the results verified that the temperature field response was uniform during the FJH synthesis process. Furthermore, this paper theoretically analyzed the feasibility of FJH to synthesize CC-S-HEA. The electrochemical test of different catalysts verified that the CC-S-HEA_{60} synthesized with optimal synthesis parameters was an excellent electrocatalyst, and it had comparable HER performance to Pt/C. Moreover, the DFT calculations revealed that S atoms on CC-S could effectively anchor metal atoms and facilitate electron transfer between the carbon substrate and HEA particles. The unique electronic structure of CC-S-HEA coordinated to maintain high electrical activity throughout the process. By calculating the ΔG_{H^*} of different catalysts, it was proved that the successful synthesis of HEA particles effectively improved the HER performance of CC-S-HEA. The convenience of synthesis, high product quality, and scalability indicated that the FJH system is one of the most promising ways to synthesize high-efficiency HEA electrocatalysts, which not only reduces energy waste but also has the potential for continuous production, providing a reference for advancing the development of nanocatalysts.

Acknowledgements

This work was supported by Key Research and Development Project of Xuzhou City (No. KC21287) and the National Natural Science Foundation of China (No. 51974307).

Electronic Supplementary Material: Supplementary material (the pictures of CC, CC-S and CC-S-HEA before and after FJH treatment, the resistivity of CC, CC-S and CC-S-HEA_{20-80}, the flash pictures of CC at different times when the FJH system is working captured by the high-speed camera; SEM and EDS images of CC-S; SEM, EDS, and XPS images of CC-HEA; SEM, EDS, and XRD images of CC-S-HEA; the differential charge density maps of CC-HEA and CC-S-HEA; the DFT model of CC, CC-S, and CC-S-HEA; the PDOS curves of different metal atoms in CC-S-HEA; and the DFT model of adsorption of H* on Pt (111)) is available in the online version of this article at https://doi.org/10.1007/s12274-023-6215-8.

References

[1] Wang, W.; Wu, Y. X.; Lin, Y. X.; Yao, J. X.; Wu, X. S.; Wu, C. Q.; Zuo, X. Q.; Yang, Q.; Ge, B. H. et al. Confining zero-valent platinum single atoms in α-MoC_{1-x} for pH-Universal hydrogen evolution reaction. *Adv. Funct. Mater.* **2022**, *32*, 2108464.

[2] Zhang, L. L.; Lei, Y. T.; Xu, W. J.; Wang, D.; Zhao, Y. F.; Chen, W. X.; Xiang, X.; Pang, X. C.; Zhang, B.; Shang, H. S. Highly active and durable nitrogen-doped CoP/CeO_2 nanowire heterostructures for overall water splitting. *Chem. Eng. J.* **2023**, *460*, 141119.

[3] Ou, G.; Fan, P. X.; Ke, X. X.; Xu, Y. S.; Huang, K.; Wei, H. H.; Yu, W.; Zhang, H. J.; Zhong, M. L.; Wu, H. et al. Defective molybdenum sulfide quantum dots as highly active hydrogen evolution electrocatalysts. *Nano Res.* **2018**, *11*, 751–761.

[4] Qie, Y. Q.; Liu, Y. X.; Kong, F. Q.; Yang, Z. L.; Yang, H. High coercivity cobalt carbide nanoparticles as electrocatalysts for hydrogen evolution reaction. *Nano Res.* **2022**, *15*, 3901–3906.

[5] Xu, J. S.; Li, R.; Yan, X. Y.; Zhao, Q. K.; Zeng, R. G.; Ba, J. W.; Pan, Q. F.; Xiang, X.; Meng, D. Q. Platinum single atom catalysts for hydrogen isotope separation during hydrogen evolution reaction. *Nano Res.* **2022**, *15*, 3952–3958.

[6] Khan, M.; Yousaf, A. B.; Chen, M. M.; Wei, C. S.; Wu, X. B.; Huang, N. D.; Qi, Z. M.; Li, L. B. Molybdenum sulfide/graphene-carbon nanotube nanocomposite material for electrocatalytic applications in hydrogen evolution reactions. *Nano Res.* **2016**, *9*, 837–848.

[7] Wu, W. Z.; Huang, Y. J.; Wang, X. Q.; Shen, P. K.; Zhu, J. L. Composition-optimized manganese phosphide nanoparticles anchored on porous carbon network for efficiently electrocatalytic hydrogen evolution. *Chem. Eng. J.* **2023**, *469*, 143879.

[8] Liu, H.; Qin, H. Y.; Kang, J. L.; Ma, L. Y.; Chen, G. X.; Huang, Q.; Zhang, Z. J.; Liu, E. Z.; Lu, H. M.; Li, J. X. et al. A freestanding nanoporous NiCoFeMoMn high-entropy alloy as an efficient electrocatalyst for rapid water splitting. *Chem. Eng. J.* **2022**, *435*, 134898.

[9] Salah, A.; Ren, H. D.; Al-Ansi, N.; Tan, H. Q.; Yu, F. Y.; Liu, Y. C.; Thamer, B. M.; Al-Salihy, A.; Zhao, L.; Li, Y. G. Dispersing small Ru nanoparticles into boron nitride remodified by reduced graphene oxide for high-efficient electrocatalytic hydrogen evolution reaction. *J. Colloid Interface Sci.* **2023**, *644*, 378–387.

[10] Xu, L.; Gu, Y.; Li, Y. Y.; Liu, H. Z.; Shang, Y. Y.; Zhu, Y. Y.; Zhou, B.; Zhu, L. H.; Jiang, X. Q. One-step preparation of molybdenum disulfide/graphene nano-catalysts through a simple Co-exfoliation method for high-performance electrocatalytic hydrogen evolution reaction. *J. Colloid Interface Sci.* **2019**, *542*, 355–362.

[11] Zhu, J.; Hu, L. S.; Zhao, P. X.; Lee, L. Y. S.; Wong, K. Y. Recent advances in electrocatalytic hydrogen evolution using nanoparticles. *Chem. Rev.* **2020**, *120*, 851–918.

[12] Chen, Z. L.; Qing, H. L.; Zhou, K.; Sun, D. L.; Wu, R. B. Metal-organic framework-derived nanocomposites for electrocatalytic hydrogen evolution reaction. *Prog. Mater. Sci.* **2020**, *108*, 100618.

[13] Liu, D. B.; Li, X. Y.; Chen, S. M.; Yan, H.; Wang, C. D.; Wu, C. Q.; Haleem, Y. A.; Duan, S.; Lu, J. L.; Ge, B. H. et al. Atomically dispersed platinum supported on curved carbon supports for efficient electrocatalytic hydrogen evolution. *Nat. Energy* **2019**, *4*, 512–518.

[14] Nemiwal, M.; Gosu, V.; Zhang, T. C.; Kumar, D. Metal organic frameworks as electrocatalysts: Hydrogen evolution reactions and overall water splitting. *Int. J. Hydrogen Energy* **2021**, *46*, 10216–10238.

[15] Shan, A. X.; Teng, X. A.; Zhang, Y.; Zhang, P. F.; Xu, Y. Y.; Liu, C. R.; Li, H.; Ye, H. Y.; Wang, R. M. Interfacial electronic structure modulation of Pt-MoS_2 heterostructure for enhancing electrocatalytic hydrogen evolution reaction. *Nano Energy* **2022**, *94*, 106913.

[16] Ji, J. P.; Zhang, Y. Q.; Tang, L. B.; Liu, C. Y.; Gao, X. H.; Sun, M. H.; Zheng, J. C.; Ling, M.; Liang, C. D.; Lin, Z. Platinum single-atom and cluster anchored on functionalized MWCNTs with ultrahigh mass efficiency for electrocatalytic hydrogen evolution. *Nano Energy* **2019**, *63*, 103849.

[17] Zhou, D.; Jiang, B.; Yang, R.; Hou, X. D.; Zheng, C. B. One-step synthesis of monodispersed Pt nanoparticles anchored on 3D graphene foams and its application for electrocatalytic hydrogen evolution. *Chin. Chem. Lett.* **2020**, *31*, 1540–1544.

[18] Gao, D. D.; Liu, R. J.; Biskupek, J.; Kaiser, U.; Song, Y. F.; Streb, C. Modular design of noble-metal-free mixed metal oxide electrocatalysts for complete water splitting. *Angew. Chem., Int. Ed.* **2019**, *58*, 4644–4648.

[19] Sun, J. S.; Wen, Z.; Han, L. P.; Chen, Z. W.; Lang, X. Y.; Jiang, Q. Nonprecious intermetallic Al_7Cu_4Ni nanocrystals seamlessly integrated in freestanding bimodal nanoporous copper for efficient hydrogen evolution catalysis. *Adv. Funct. Mater.* **2018**, *28*, 1706127.

[20] Feng, D. Y.; Dong, Y. B.; Nie, P.; Zhang, L.; Qiao, Z. A. CoNiCuMgZn high entropy alloy nanoparticles embedded onto graphene sheets via anchoring and alloying strategy as efficient electrocatalysts for hydrogen evolution reaction. *Chem. Eng. J.* **2022**, *430*, 132883.

[21] Pedersen, J. K.; Batchelor, T. A. A.; Bagger, A.; Rossmeisl, J. High-entropy alloys as catalysts for the CO_2 and CO reduction reactions. *ACS Catal.* **2020**, *10*, 2169–2176.

[22] Peng, H. L.; Xie, Y. C. Z.; Xie, Z. C.; Wu, Y. F.; Zhu, W. K.; Liang, S. Q.; Wang, L. B. Large-scale and facile synthesis of a porous high-entropy alloy CrMnFeCoNi as an efficient catalyst. *J. Mater. Chem. A* **2020**, *8*, 18318–18326.

[23] Li, K.; Chen, W. Recent progress in high-entropy alloys for catalysts: Synthesis, applications, and prospects. *Mater. Today Energy* **2021**, *20*, 100638.

[24] Chen, Z. Q.; Wen, J. B.; Wang, C. H.; Kang, X. W. Convex cube-shaped $Pt_{34}Fe_5Ni_{20}Cu_{31}Mo_9Ru$ high entropy alloy catalysts toward

high-performance multifunctional electrocatalysis. *Small* **2022**, *18*, 2204255.

[25] Lei, Y. T.; Zhang, L. L.; Xu, W. J.; Xiong, C. L.; Chen, W. X.; Xiang, X.; Zhang, B.; Shang, H. S. Carbon-supported high-entropy Co-Zn-Cd-Cu-Mn sulfide nanoarrays promise high-performance overall water splitting. *Nano Res.* **2022**, *15*, 6054–6061.

[26] Ma, P. Y.; Zhao, M. M.; Zhang, L.; Wang, H.; Gu, J. F.; Sun, Y. C.; Ji, W.; Fu, Z. Y. Self-supported high-entropy alloy electrocatalyst for highly efficient H_2 evolution in acid condition. *J. Materiomics* **2020**, *6*, 736–742.

[27] Li, H. D.; Han, Y.; Zhao, H.; Qi, W. J.; Zhang, D.; Yu, Y. D.; Cai, W. W.; Li, S. X.; Lai, J. P.; Huang, B. L. et al. Fast site-to-site electron transfer of high-entropy alloy nanocatalyst driving redox electrocatalysis. *Nat. Commun.* **2020**, *11*, 5437.

[28] Al Bacha, S.; Pighin, S. A.; Urretavizcaya, G.; Zakhour, M.; Nakhl, M.; Castro, F. J.; Bobet, J. L. Effect of ball milling strategy (milling device for scaling-up) on the hydrolysis performance of Mg alloy waste. *Int. J. Hydrogen Energy* **2020**, *45*, 20883–20893.

[29] Dong, Y.; Duan, S. G.; Huang, X.; Li, C. Q.; Zhang, Z. R. Excellent strength-ductility synergy in as-cast $Al_{0.6}CoCrFeNi_2Mo_{0.08}V_{0.04}$ high-entropy alloy at room and cryogenic temperatures. *Mater. Lett.* **2021**, *294*, 129778.

[30] Zhang, N.; Feng, X. B.; Rao, D. W.; Deng, X.; Cai, L. J.; Qiu, B. C.; Long, R.; Xiong, Y. J.; Lu, Y.; Chai, Y. Lattice oxygen activation enabled by high-valence metal sites for enhanced water oxidation. *Nat. Commun.* **2020**, *11*, 4066.

[31] Ud Din, M. A.; Saleem, F.; Ni, B.; Yong, Y.; Wang, X. Porous tetrametallic PtCuBiMn nanosheets with a high catalytic activity and methanol tolerance limit for oxygen reduction reactions. *Adv. Mater.* **2017**, *29*, 1604994.

[32] Dai, W. J.; Lu, T.; Pan, Y. Novel and promising electrocatalyst for oxygen evolution reaction based on MnFeCoNi high entropy alloy. *J. Power Sources* **2019**, *430*, 104–111.

[33] Ortega, S.; Ibáñez, M.; Liu, Y.; Zhang, Y.; Kovalenko, M. V.; Cadavid, D.; Cabot, A. Bottom-up engineering of thermoelectric nanomaterials and devices from solution-processed nanoparticle building blocks. *Chem. Soc. Rev.* **2017**, *46*, 3510–3528.

[34] Wyss, K. M.; Chen, W. Y.; Beckham, J. L.; Savas, P. E.; Tour, J. M. Holey and wrinkled flash graphene from mixed plastic waste. *ACS Nano* **2022**, *16*, 7804–7815.

[35] Algozeeb, W. A.; Savas, P. E.; Yuan, Z.; Wang, Z.; Kittrell, C.; Hall, J. N.; Chen, W. Y.; Bollini, P.; Tour, J. M. Plastic waste product captures carbon dioxide in nanometer pores. *ACS Nano* **2022**, *16*, 7284–7290.

[36] Huang, P. F.; Zhu, R. T.; Zhang, X. X.; Zhang, W. J. Effect of free radicals and electric field on preparation of coal pitch-derived graphene using flash joule heating. *Chem. Eng. J.* **2022**, *450*, 137999.

[37] Liu, S. L.; Shen, Y.; Zhang, Y.; Cui, B. H.; Xi, S. B.; Zhang, J. F.; Xu, L. Y.; Zhu, S. Z.; Chen, Y. N.; Deng, Y. D. et al. Extreme environmental thermal shock induced dislocation-rich Pt nanoparticles boosting hydrogen evolution reaction. *Adv. Mater.* **2022**, *34*, 2106973.

[38] Liu, C.; Shen, Y.; Zhang, J. F.; Li, G.; Zheng, X. R.; Han, X. P.; Xu, L. Y.; Zhu, S. Z.; Chen, Y. N.; Deng, Y. D. et al. Multiple twin boundary-regulated metastable Pd for ethanol oxidation reaction. *Adv. Energy Mater.* **2022**, *12*, 2103505.

[39] Luo, J. W.; Zhang, J. C.; Guo, Z. X.; Liu, Z. D.; Dou, S. M.; Liu, W. D.; Chen, Y. N.; Hu, W. B. Recycle spent graphite to defect-engineered, high-power graphite anode. *Nano Res.* **2023**, *16*, 4240–4245.

[40] Zeng, C. H.; Duan, C. P.; Guo, Z. X.; Liu, Z. D.; Dou, S. M.; Yuan, Q. Y.; Liu, P.; Zhang, J. C.; Luo, J. W.; Liu, W. D. et al. Ultrafastly activated needle coke as electrode material for supercapacitors. *Prog. Nat. Sci.* **2022**, *32*, 786–792.

[41] Chen, Y. N.; Egan, G. C.; Wan, J. Y.; Zhu, S. Z.; Jacob, R. J.; Zhou, W. B.; Dai, J. Q.; Wang, Y. B.; Danner, V. A.; Yao, Y. G. et al. Ultra-fast self-assembly and stabilization of reactive nanoparticles in reduced graphene oxide films. *Nat. Commun.* **2016**, *7*, 12332.

[42] Zhao, J. H.; Wang, Z. Y.; Fang, X. Y.; Yang, L.; Wu, C. Q.; Gan, W.; Zhou, Y.; Shan, L.; Lin, Y. X. Fast joule heating synthesis of NiCoFeCrMo high-entropy alloy embedded in graphene for water oxidation. *J. Alloys Compd.* **2023**, *966*, 171535.

[43] Laidler, K. J. The development of the arrhenius equation. *J. Chem. Educ.* **1984**, *61*, 494.

[44] Welch, G. R. Some problems in the usage of gibbs free energy in biochemistry. *J. Theor. Biol.* **1985**, *114*, 433–446.

[45] Wei, S.; Wan, C. C.; Li, X. G.; Su, J. H.; Cheng, W. J.; Chai, H. Y.; Wu, Y. Q. Constructing N-doped and 3D hierarchical porous graphene nanofoam by plasma activation for supercapacitor and Zn ion capacitor. *iScience* **2023**, *26*, 105964.

[46] Wahab, H.; Jain, V.; Tyrrell, A. S.; Seas, M. A.; Kotthoff, L.; Johnson, P. A. Machine-learning-assisted fabrication: Bayesian optimization of laser-induced graphene patterning using *in-situ* Raman analysis. *Carbon* **2020**, *167*, 609–619.

[47] Xu, X.; Du, Y. K.; Wang, C. H.; Guo, Y.; Zou, J. W.; Zhou, K.; Zeng, Z.; Liu, Y. Y.; Li, L. Q. High-entropy alloy nanoparticles on aligned electronspun carbon nanofibers for supercapacitors. *J. Alloys Compd.* **2020**, *822*, 153642.

[48] Yao, R. Q.; Zhou, Y. T.; Shi, H.; Wan, W. B.; Zhang, Q. H.; Gu, L.; Zhu, Y. F.; Wen, Z.; Lang, X. Y.; Jiang, Q. Nanoporous surface high-entropy alloys as highly efficient multisite electrocatalysts for nonacidic hydrogen evolution reaction. *Adv. Funct. Mater.* **2021**, *31*, 2009613.

[49] Liu, C.; Zhu, H.; Lu, S. L.; Duan, F.; Du, M. L. High entropy alloy nitrides with integrated nanowire/nanosheet architecture for efficient alkaline hydrogen evolution reactions. *New J. Chem.* **2021**, *45*, 22255–22260.

[50] Moradi, M.; Hasanvandian, F.; Bahadoran, A.; Shokri, A.; Zerangnasrabad, S.; Kakavandi, B. New high-entropy transition-metal sulfide nanoparticles for electrochemical oxygen evolution reaction. *Electrochim. Acta* **2022**, *436*, 141444.

[51] Paulraj, G.; Venkatesh, P. S.; Dharmaraj, P.; Gopalakrishnan, S.; Jeganathan, K. Stable and highly efficient MoS_2/Si NWs hybrid heterostructure for photoelectrocatalytic hydrogen evolution reaction. *Int. J. Hydrogen Energy* **2020**, *45*, 1793–1801.

[52] Chandrasekaran, P.; Edison, T. N. J. I.; Sethuraman, M. G. Electrocatalytic performance of carbon dots/palladium nanoparticles composite towards hydrogen evolution reaction in acid medium. *Int. J. Hydrogen Energy* **2020**, *45*, 28800–28811.

[53] Tan, Y.; Wei, Y. K.; Liang, K. X.; Wang, L. Y.; Zhang, S. H. Facile *in-situ* deposition of Pt nanoparticles on nano-pore stainless steel composite electrodes for high active hydrogen evolution reaction. *Int. J. Hydrogen Energy* **2021**, *46*, 26340–26346.

[54] Lu, Y.; Geng, S. H.; Wang, S. J.; Rao, S. C.; Huang, Y.; Zou, X. L.; Zhang, Y. W.; Xu, Q.; Lu, X. G. Electrodeposition of Ni-Mo-Cu coatings from roasted nickel matte in deep eutectic solvent for hydrogen evolution reaction. *Int. J. Hydrogen Energy* **2019**, *44*, 5704–5716.

[55] Wang, S. Q.; Xu, B. L.; Huo, W. Y.; Feng, H. C.; Zhou, X. F.; Fang, F.; Xie, Z. H.; Shang, J. K.; Jiang, J. Q. Efficient FeCoNiCuPd thin-film electrocatalyst for alkaline oxygen and hydrogen evolution reactions. *Appl. Catal. B: Environ.* **2022**, *313*, 121472.

[56] Liu, Y.; Ma, C.; Zhang, Q. H.; Wang, W.; Pan, P. F.; Gu, L.; Xu, D. D.; Bao, J. C.; Dai, Z. H. 2D electron gas and oxygen vacancy induced high oxygen evolution performances for advanced Co_3O_4/CeO_2 nanohybrids. *Adv. Mater.* **2019**, *31*, 1900062

[57] Jin, J.; Yin, J.; Liu, H. B.; Huang, B. L.; Hu, Y.; Zhang, H.; Sun, M. Z.; Peng, Y.; Xi, P. X.; Yan, C. H. Atomic sulfur filling oxygen vacancies optimizes H absorption and boosts the hydrogen evolution reaction in alkaline media. *Angew. Chem., Int. Ed.* **2021**, *133*, 14236–14242.

[58] Zhao, X.; Li, X. Y.; Xiao, D. D.; Gong, M. X.; An, L. L.; Gao, P. F.; Yang, J. L.; Wang, D. L. Isolated Pd atom anchoring endows cobalt diselenides with regulated water-reduction kinetics for alkaline hydrogen evolution. *Appl. Catal. B: Environ.* **2021**, *295*, 120280.

[59] Shaker, T.; Mehdipour, H.; Moshfegh, A. Z. Low loaded MoS_2/carbon cloth as a highly efficient electrocatalyst for hydrogen evolution reaction. *Int. J. Hydrogen Energy* **2022**, *47*, 1579–1588.